Supplementary material for

An analytical framework reduces cloud feedback uncertainty by linking percentage cloud change to surface ocean warming patterns

Jian Ma, Jing Feng, Hui Su, Matthew Collins, In-Sik Kang, Masahiro Watanabe, Jianping Li, and Yinding Zhang

Jian Ma
Email: Jian.Ma@SJTU.edu.cn

This PDF file includes:

Supplementary Text

Dual mechanisms for the cloud fraction change. The ensemble-mean changes in cloud fraction (δC, shading in Fig. S1 *A* to *C*) are much stronger from 40°S to 40°N (roughly the extended tropics, including the subtropics) than in the extratropics (1). This is particularly true for changes in high and low clouds, which generally follow the SST change patterns (T^*, relative SST increase deviating from the tropical mean warming), with r_s of 0.46 and -0.48, respectively. With respect to the SST (Fig. S1*D*), the opposite signs of r_s reflect the distinct dynamics between these cloud types. Briefly, a positive T^* value is associated with enhanced convection, which increases high clouds (2), and with weakened boundary layer stability, which reduces low clouds (3). Equivalently, cloud tops can rise or fall (4–7), depending on the sign of fraction changes controlled by the SST patterns.

However, the cloud fraction changes are not entirely determined by the SST patterns, and there are spatial shifts that vary considerably between cloud types. In particular, low clouds decrease greatly over the eastern basins in the Pacific and Atlantic Oceans, while high clouds increase along the equator, except over the Indo-Pacific warm pool where a strong reduction zone extends towards the subtropics. Most pronounced changes occur where the climatological cloud fraction is large, e.g., the horizontal correlation between the ensemble-mean δC and C is large (-0.44) for low clouds. Indeed, these δC patterns are covered by the stippled areas in Fig. S1 where C is more than 20%. In addition, strong intermodel spreads (contours) of δC also appear in these areas and are highly correlated in space with the ensemble-mean C for high (0.6), middle (0.52), and low (0.79) clouds. These tropics-wide patterns manifest as beta-style scaling and relate the strength of the fraction changes to the present-day amounts of clouds, not only at low levels but for all cloud types.

Such climatological modulation complicates the dynamical interpretation of the cloud fraction change by generating a large strength disparity between cloud types. In particular, middle cloud δC is confined by moderate C values in a small region of the subtropical southeastern Pacific, while leaving an order of magnitude lower change in the vast remaining regions compared to those in high and low clouds. This is more evident in the vertical transects (Fig. S2 *A* and *B*), where the ensemble-mean δC exhibits a strong contrast between the mid-troposphere (440–680 hPa) and other altitudes, which is consistent with the intermodel spread. As a measure of the strength of δC, the spread appears to be closely related to the ensemble-mean C ($r_s \geq 0.76$). In sum, Fig. S1 qualifies that the fraction changes in all types of clouds are governed by the SST

patterns in terms of sign and by the climatological amounts in terms of strength, which apparently integrates the pattern effect and beta scaling scheme, respectively.

Intermodel uncertainty in cloud sensitivity and feedback. All individual simulations show strong spatial correlations between T^* and Δ (Fig. S3*A*), with ensemble means of 0.55 and -0.53 in the high and low cloud cases, respectively, which are about 0.1 larger than those for δC (Fig. S3*B*). This robustly demonstrates the cross-model consistency of the proportional warmer-get-higher paradigm; nevertheless, r_s can vary between models by more than a third of the ensemble mean. Furthermore, the percentage sensitivity α is antisymmetric between high and low clouds (r_m = -0.56), implying a concurrent strength of T^* control between the cloud types in a given model. Indeed, its very large range even two times of the mean (e.g., -2 to -25% K^{-1} in Fig. 3) can be attributed to a major factor (besides SST), the stability indices controlling the tropical-oceanic low clouds (3, 8–10). As shown in Fig. S4, they are reshaped by the SST in spatial patterns for 52–76%, and their typically studied spatial-mean changes can explain up to 38% of the intermodel variability in α. Thus, α is a comprehensive representation of atmospheric dynamics revealed from a new percentage perspective, which can inclusively constrain key cloud-controlling factors (11–14).

In the CMIP projections, the original global λ is 0.11±0.13, 0.12±0.37, 0.26±0.3, and 0.49±0.65 W m^{-2} K^{-1} (90% confidence) for high, middle, low, and total clouds, respectively (Fig. S5). Middle (44%) and non-obscured low (43%) clouds dominate the intermodel spread of total cloud λ, mainly due to their diverse changes in shortwave radiation (15). High clouds considerably affect both solar reflection and infrared absorption, but they tend to offset each other with an intermodel anticorrelation (r_m = -0.96), leaving a small contribution (13%) to the net λ uncertainty. Since low clouds are one dominator of total cloud feedback, we take them as the main example for examining the intermodel variability (Fig. 3) with our percentage analytical framework.

Interestingly (Fig. S8), total cloud feedback in the tropics has a 37% covariance (r_m = 0.61) with the extratropical feedback, and hence controls 85% of the global uncertainty with r_m of 0.92. For the main stream of models, the α of non-obscured low clouds is well correlated (-0.59) with the tropical feedback, accounting for 35% of the intermodel range (Fig. S8*C*). These robustly couple α to the global λ for total clouds (r_m = -0.69) in Fig. 3*C*, explaining 48% of the intermodel range. Mainly due to low cloud dissipation in the extratropics, three outlier models contain weak α but strong λ to relax their correlation by ~30%, over both the tropics and the globe. Fortunately, a later investigation will show that their effect is marginal, which supports the robustness of our

constraint. Even when they are included, high cloud α is strongly correlated (0.74) with the global λ, explaining 55% of the variance.

Fractional kernels and SVD patterns. Indeed, the cloud climatology C modulates the fractional kernels to feature much stronger spatial variations in Fig. S9 compared to the radiative kernels K (15). The shortwave kernel integrates reflective cooling by total clouds, and the longwave kernel inherits infrared warming by high clouds. An r_s of -0.73 between them indicates the radiative offset in high clouds, so that solar reflection by low clouds dominates the net kernel, with a minor contribution from mid-level clouds. Thus, a pronounced net γK appears over the eastern basins, with maximum spreads around the equatorical oceans, reflecting biases in the cloud simulation (16, 17) and introducing strong uncertainty into the global cloud feedback via these fractional kernels. Replacing the CMIP cloud fraction with the MODIS observations can remove this intermodel variability, leaving a minor spread in $\gamma_o K$ only around the Tibetan Plateau due to the surface shortwave albedo. The replacement also corrects a few biases in the simulation, although the net $\overline{\gamma K}$ exhibits quite good skills to resemble $\gamma_o \overline{K}$ with r_s = 0.79. These include an underestimated fraction and elevated tops of low clouds and an overestimated fraction of middle and high clouds, due to an upward error in the retrieval algorism of cloud height from the satellite simulator in the CMIP models (18).

We apply the SVD analyses to obtain covariant modes between the global T^* and Δ, for both the scaled and unscaled cases (*Methods*). The two leading SVD modes (Fig. S11) explain 45% and 31% of the variance in the unscaled Δ' from Eq. **9**, and switch ranks in the scaled case to reflect the efficiency of our substitution. In the horizontal distributions, the tropical clouds are strongly correlated with the SSTs, e.g., the non-obscured low clouds in modes 1 (-0.57) and 2 (-0.5), and high clouds in mode 2 (0.56). The zonal-mean modes also feature high r_s values: 0.46/0.56 for high clouds over the Pacific/Indian Ocean, and -0.45/-0.93/-0.55 for low clouds over the Pacific/Atlantic/Indian Ocean in mode 1; 0.83/0.54 for high clouds over the Pacific/Indian Ocean, and -0.37/-0.43 for low clouds over the Pacific/Atlantic in mode 2.

Optical depth and outlier models. Our percentage analytical framework explicitly addresses cloud feedback caused by amount and altitude changes; however, thin-thick cloud transitions also have a comparable uncertainty contribution (12, 19). Therefore, it is necessary to decompose cloud feedback (20) and examine whether our constraint has an implicit effect on optical depth feedback. Fig. S14 compares the feedback components and shows that their uncertainties are thoroughly reduced in all cloud types, although not always in each stage. The percentage uncertainty (90% confidence) reductions in the global high, middle, low, and total cloud feedback are, respectively: 24%, 70%, 36%,18% for cloud amount; 46%, 11%, 58%, and 34% for altitude;

33%, 72%, 54%, and 40% for optical depth. Surprisingly, optical depth is the largest contributor to constraining total cloud feedback, with a strong effect for each cloud type; in contrast, amount feedback is only substantially constrained for middle clouds. In summary, our method is most effective for cloud altitude and optical depth feedbacks, rather than amount feedback as expected from a constraint on cloud fraction change.

Thus, although we simply sum over all optical depths, this feedback can be implicitly adjusted by using our constraint in a variety of ways. First, the observational replacement of the climatological cloud fraction applies to the 7-by-7 clisccp, which can correct the ground truth for the optical depth change. Second, the amount change relies on a weighted average of the percentage change across the p-τ bins, and the rest of the percentage change remains in the p-τ matrix (submatrices) for total clouds (cloud types). Hence, the 7-level sensitivity substitution of the 7-by-7 Δ would affect both the altitude and optical depth feedback by scaling the amount change. Last, the constricted models also facilitate the most likely SST patterns to avoid some unrealistic optical depth changes. As a result, Fig. S14 indicates that our constraint is sufficiently effective, leaving uncorrected parts in the opacity effect and stability change for future studies.

We then formally examine the outlier effects of HadGEM3-GC3.1-LL, UKESM1.0-LL, and UKESM1.1-LL from CMIP6. Without them, the global total, low, middle, and high cloud feedbacks (90% confidence) are, respectively: 0.41±0.67, 0.22±0.28, 0.09±0.38, and 0.1±0.14 W m^{-2} K^{-1} for the original; 0.41±0.31, 0.28±0.24, 0.06±0.11, and 0.07±0.14 W m^{-2} K^{-1} for the substituted; 0.46±0.27, 0.33±0.21, 0.07±0.09, 0.06±0.06 W m^{-2} K^{-1} for the constrained feedback. It can be clearly seen that this outlier removal has little effect on all uncertainties, and its most prominent impact is to reduce the ensemble means. For example, total cloud feedback drops by 0.08, 0.04, and 0.03 W m^{-2} K^{-1}, which decrease from the original to the constrained feedback. This shows the robustness of our constraint, as it is the least affected. Furthermore, the main contributors are higher-level clouds, while low clouds are unaffected. Relative to the uncertainty, this one-ninth reduction is insignificant, so we prefer to include the outliers in our final results.

Methods

Intermodel statistical analysis. This statistical analysis explores the dynamical interpretations for tracing the valuable sources of uncertainty, e.g., the contribution of the percentage cloud sensitivity to cloud feedback. Regular statistics use spatiotemporal fields as inputs, but here we replace the time axis with the model series to perform intermodel analysis. In particular, the intermodel correlations and regressions are performed for cloud feedback, and the variances explained by different factors are estimated as the exclusive R^2 (to be introduced) for the total

effect. In addition, Student's *t*-tests are used to assess the confidence of the correlations using the following formula:

$$t_r = \frac{\sqrt{n-3}}{2} \ln\left(\frac{1+r}{1-r}\right),$$

where t_r is the test statistic derived from the correlation r (r_s or r_m) and the sample size n. All of r_m across the 21 models are above the 90% confidence level. Except for the (percentage) fraction change in total and middle clouds, all of r_s pass the 99.99% confidence tests because the tropical sample size is at least 4430 for the SST patterns or 270 for the zonal-mean cloud fraction.

As an extension of the EOF, the SVD analysis (21, 22) is a popular multivariate statistical method, which uses two variables as inputs to identify their patterns with the maximum covariance. Here we perform intermodel SVD (23, 24) to extract the effect of the SST patterns on the regional cloud changes with their covariant modes. Two sets of SVDs are applied to the monthly intermodel anomalies of Δ and Δ_s in Eqs. **5** and **6**, respectively. They are both between the global T^* (4-D: x, y, month, model) and cloud changes (6-D: x, y, p, τ, month, model) in terms of the percentage for the extended tropics (40°S–40°N) and the fraction for the outside extratropics. All of the variables have been concatenated into 2-D matrices with dimensions only along the model and the combinations of others, and the ensemble mean is removed for each grid box. A covariance matrix $Co = \Delta^t T^*/N$ is then constructed by eliminating the common model dimension, where t denotes the transpose operator and N represents the number of models.

The SVD function converts Co into a tuple of three arrays E, Σ, and F. Each column in E contains a singular vector for Δ, as does F for T^*, while Σ contains the singular values not used here. These orthonormal singular vectors are identified as the spatial modes and are projected onto each of the variables to define the corresponding PCs, which are also model-dependent. We then use the fractional kernels to compute the partial feedback due to the cloud patterns in each of the SVD modes, and we multiply it by the corresponding PC. This reconstructs the T^*-related intermodel variability in cloud feedbacks associated with these modes, which are ranked according to the individual variances (direct R^2) they explain for the intermodel uncertainty in the total cloud feedback. Finally, the multi-model partial feedbacks reconstructed by the leading SVD modes are linearly combined to quantify their cumulative variance (25) using the exclusive R^2 method below.

Variances explained by linearly interdependent factors. Here we develop an exclusive R^2 method to solve the overfitting problem in the variance explanations of the linearly interdependent factors for the cloud type decompositions and uncertainty attributions. For example, the sum of the variances (direct R^2) explained by the cloud types exceeds 1 for the global shortwave

feedback (Fig. S5*A*), due to the strong negative correlation of the percetage sensitivity between high and low clouds. To correct this, we need to remove the part that is repeatedly counted in the different factors due to their linear dependence. This study involves the situations with 2–4 factors.

$Z = A + B$ is the simplest case, with two factors. The results of the exclusive R^2 method are denoted as R_A^2 and R_B^2 for A and B, respectively, and the direct R^2 values (squared correlations) are denoted as $R^2(Z, A)$ and $R^2(Z, B)$. The repetitive part between A and B is double counted (2 × 1) in $R^2(Z, A) + R^2(Z, B)$, so it is expressed as $R_{AB}^2 = \frac{R^2(Z,A)+R^2(Z,B)-1}{2}$. With the sum guaranteed to be 1, the exclusive R^2 can be obtained as follows:

$$\begin{cases} R_A^2 = R^2(Z, A) - R_{AB}^2 = \frac{1+R^2(Z,A)-R^2(Z,B)}{2} \\ R_B^2 = R^2(Z, B) - R_{AB}^2 = \frac{1-R^2(Z,A)+R^2(Z,B)}{2} \end{cases}.$$

In the three-factor case, the common part between A, B, and C is overcounted by 6 (3 × 2) times in $R^2(Z, A) + R^2(Z, B) + R^2(Z, C)$, and that between any two factors is counted twice. For four factors, the overcounting of the part common to all of them increases to 12 (4 × 3), and those for fewer factors remain the same as in the simpler cases. Consequently, the maximum overcounting of the common part would reach $i \times (i - 1)$ in the case with i factors. All of the situations can be treated in a similar way to the two-factor case, although the mathematical procedures should become increasingly complicated.

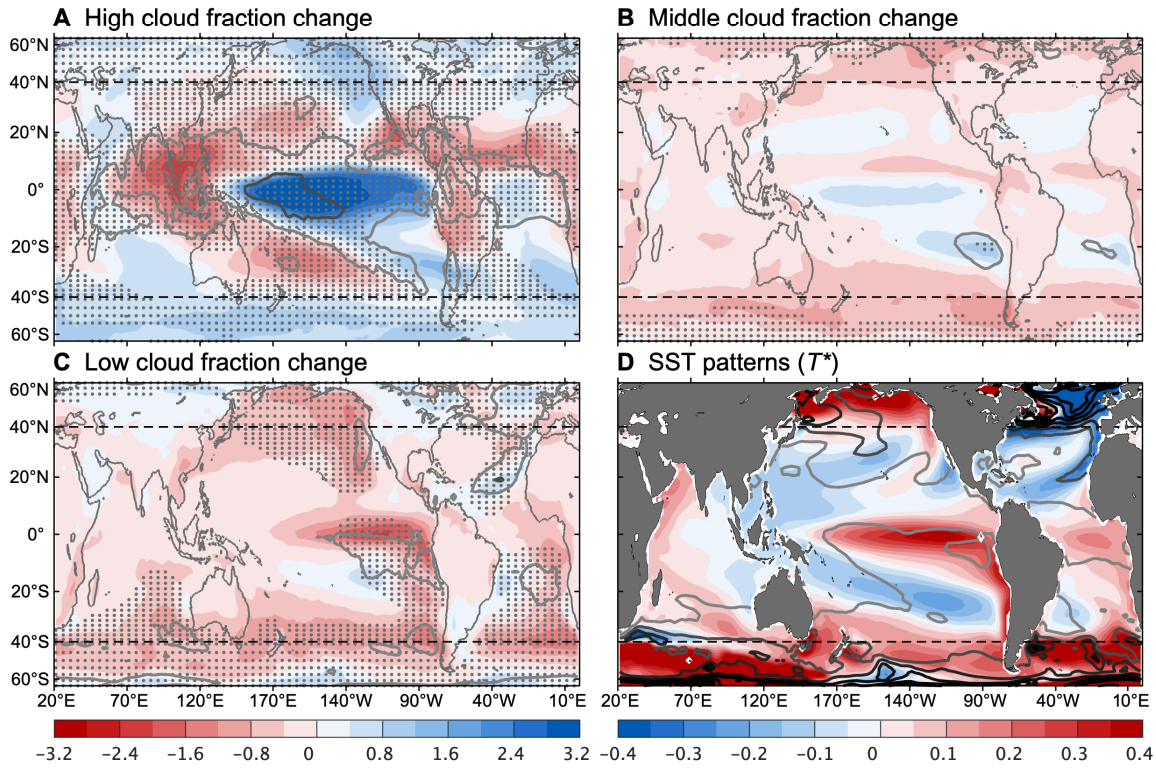

Fig. S1. Comparisons of the horizontal distributions between (*D*) the SST patterns T^* (K) and the cloud fraction change $\boldsymbol{\delta C}$ (%) for (*A*) high, (*B*) middle, and (*C*) low clouds. The ensemble mean is shown by the shading, with cloud and SST changes using the left and right color bars in opposite schemes, respectively. The intermodel spread is presented by the contours (CI: 1% for $\boldsymbol{\delta C}$ and 0.125 K for T^*; darker indicates a greater value). The stippling in (*A* to *C*) denotes the regions with a climatological cloud fraction of >20%, and the dashed lines mark the extended tropics including the subtropics (40°S–40°N). Here we use the 21 CMIP simulations normalized by the global-mean surface (air) warming.

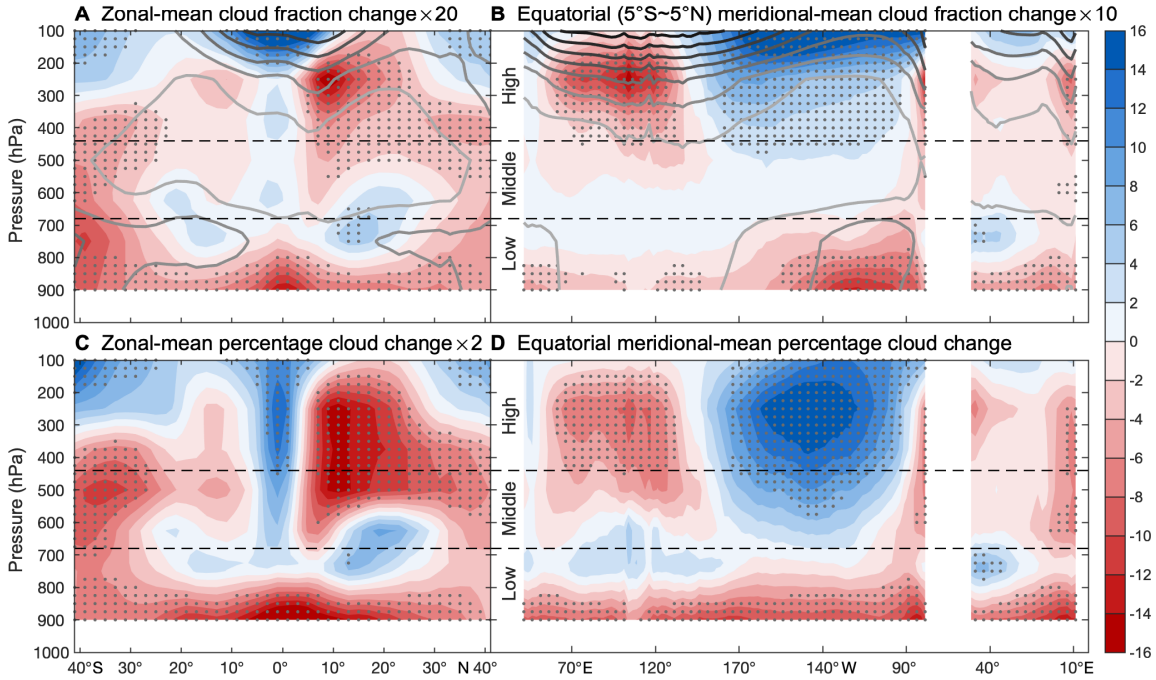

Fig. S2. Comparisons of the oceanic (*A* and *C*) zonal means and (*B* and *D*) equatorial (5°S–5°N) meridional means between (*A* and *B*) the cloud fraction change $\overline{\delta C}$ (shading, %) and (*C* and *D*) the percentage change in cloud fraction $\overline{\Delta}$ (shading, %). The stippling indicates that the ensemble mean is beyond the intermodel spread, and the background cloud climatology is shown in (*A* and *B*) as contours (CI: 5%; darker indicates a greater value). Here we use the 21 CMIP simulations normalized by the global-mean surface air warming.

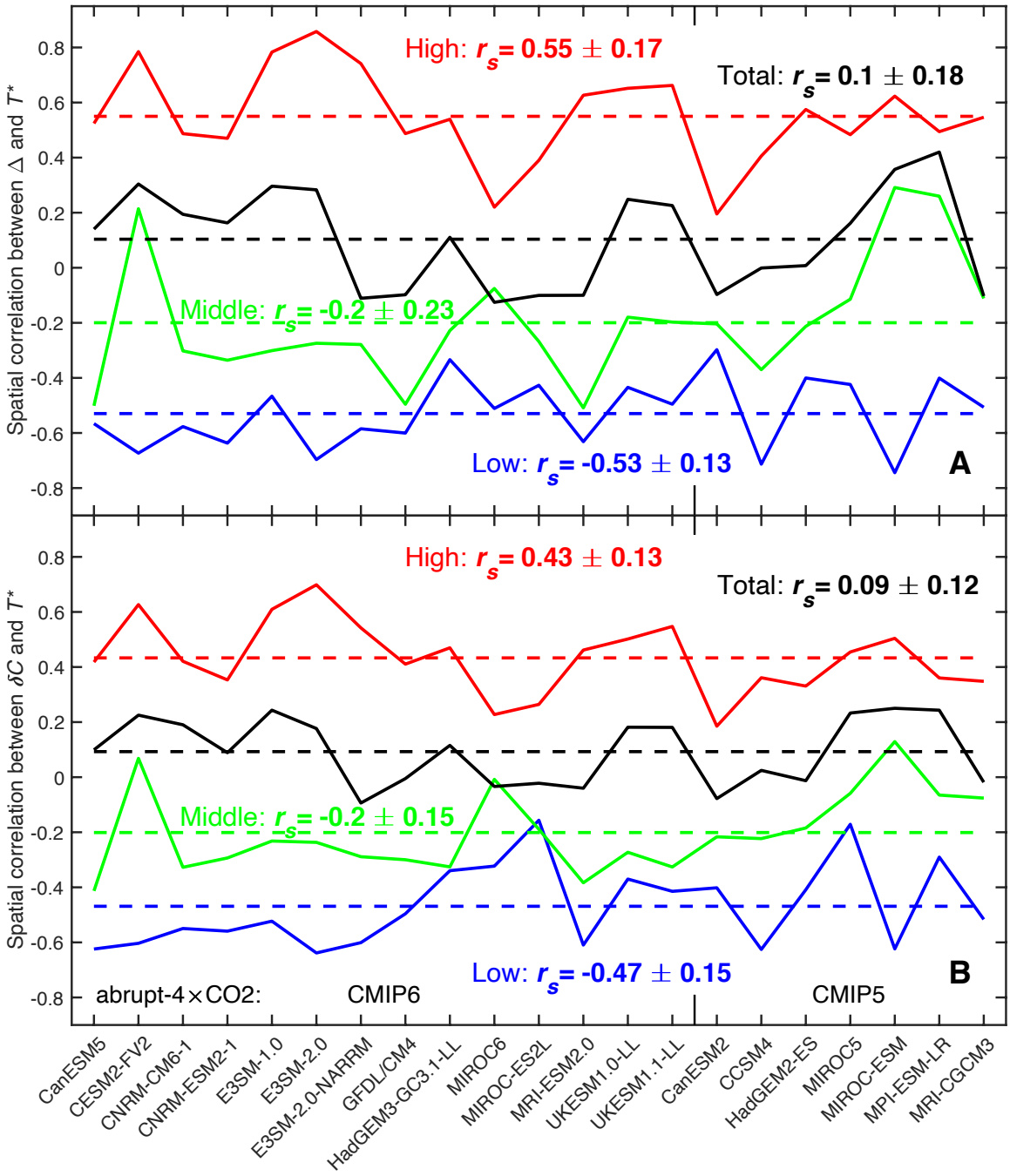

Fig. S3. Spatial correlations in the individual models (solid lines) between the SST patterns *T** and (*A*) the percentage change Δ, (*B*) fraction change δC in total (black) and specific types (color) of clouds. The dashed lines represent the ensemble means of the solid lines, and their values are marked with the intermodel spreads. Here we use the 21 CMIP simulations normalized by the global-mean surface (air) warming.

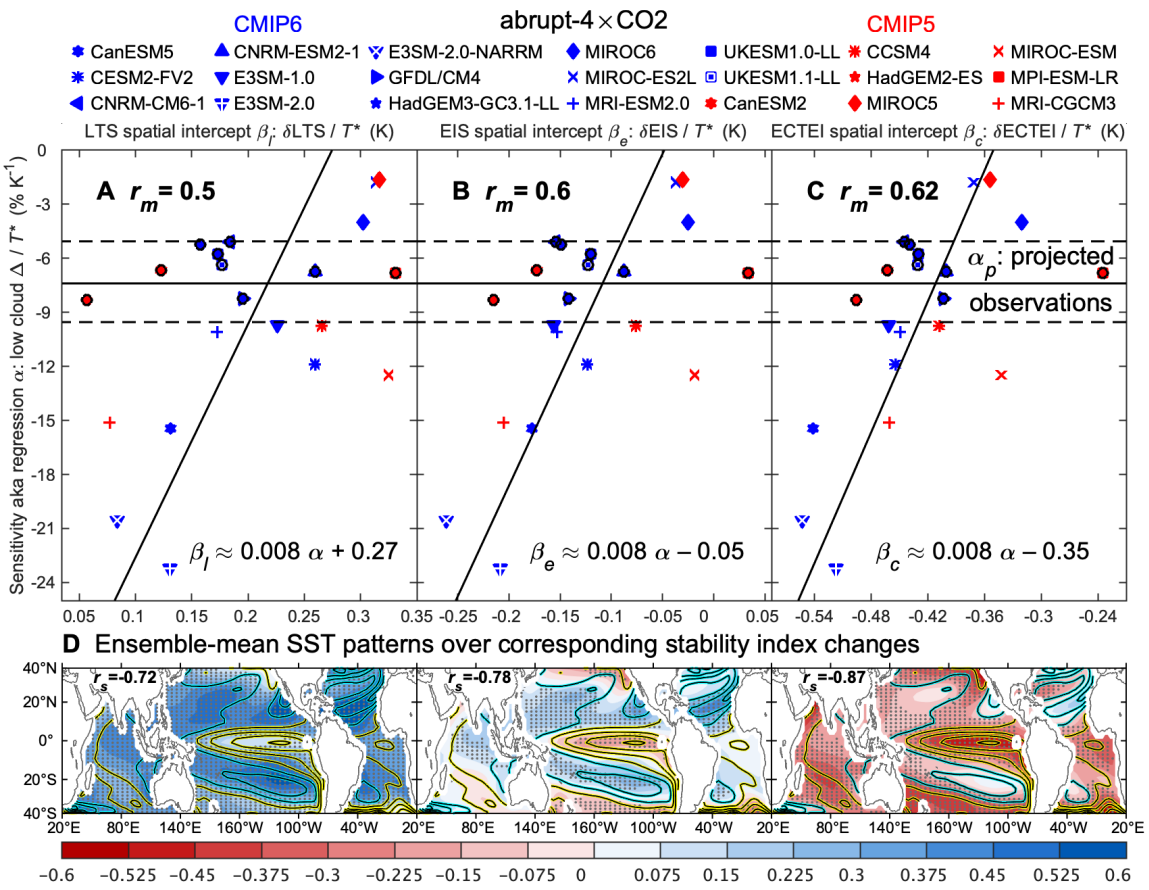

Fig. S4. Same as in Fig. 3 but (*A* to *C*) for the tropical relationships between the percentage sensitivity (α) of low clouds (% K^{-1}) and the intercepts (K) in the spatial regression of (*D*) the stability index changes against the SST patterns. Calculated over the oceans, the stability indices include: the lower-tropospheric stability (LTS), defined as the 700–1000 hPa difference in the potential temperature (*A*); the estimated inversion strength (EIS), which eliminates the lapse rate change in the free troposphere (*B*); and the estimated cloud-top entrainment index (ECTEI), which incorporates a cloud-top entrainment criterion (*C*). Using the same style as in the left panel in Fig. 1, (*D*) compares their regional changes (shading, K) with the SST patterns (contours, K) in the ensemble mean. It should be noted that the intermodel regressions keep *y*-*x* across (*A* to *C*).

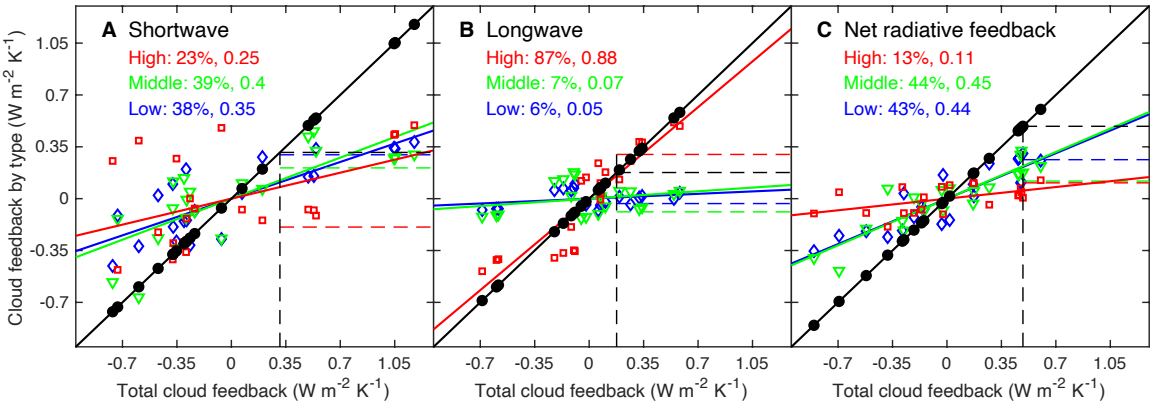

Fig. S5. Intermodel scatterplots of the global radiative feedback λ (W m^{-2} K^{-1}) for total clouds and that by type (color) for the (*A*) shortwave, (*B*) longwave, and (*C*) net radiation. For each feedback, the symbols mark the anomalies of individual models that deviate from the ensemble mean, represented by a dashed line. Black dots compare the sum of the cloud types to total clouds, which lies exactly along the black $y = x$ line. The feedback variances (exclusive R^2 in *Methods*, %) explained by the specific cloud types are listed with the slopes in the corresponding regressions. Here we use the monthly-mean cloud radiative kernels and 21 CMIP simulations normalized by the global-mean surface air warming.

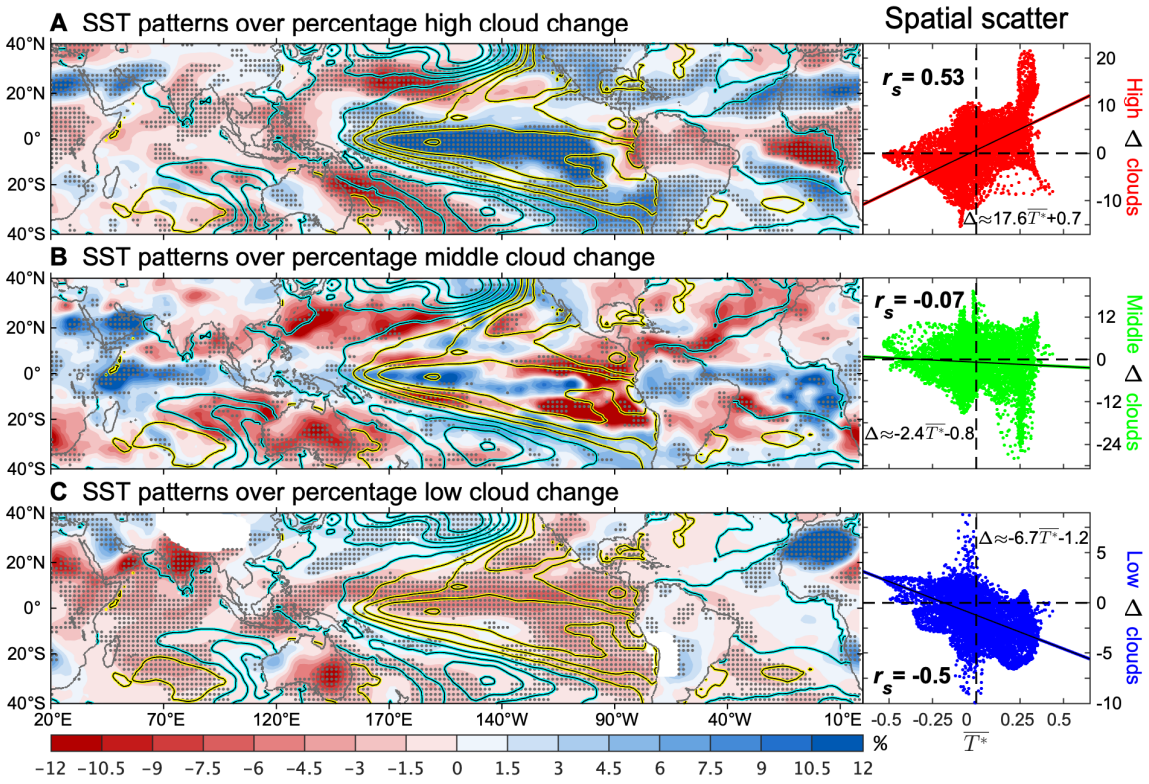

Fig. S6. Same as in Fig. 1 but computed with the MODIS clouds and the averaged SST observations for 2003–2022 using the LIM. The stippling indicates that the trend mode is beyond the spread in the LIM noise perturbations.

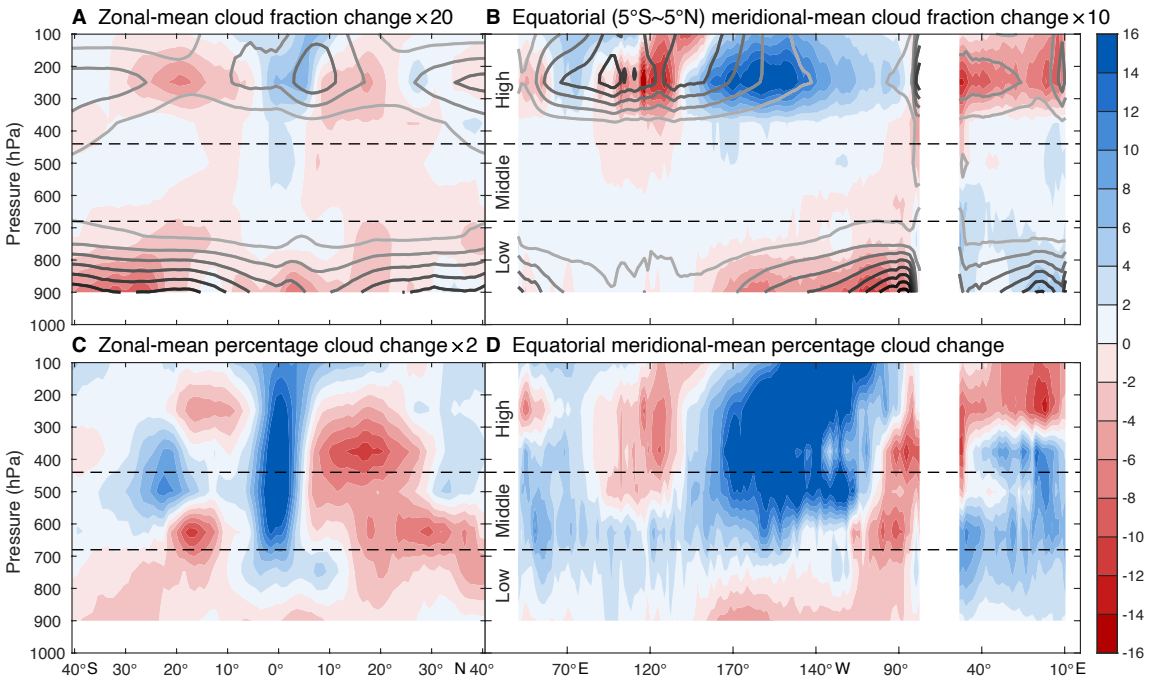

Fig. S7. Same as in Fig. S2 but computed using the MODIS cloud observations for 2003–2022 and the LIM.

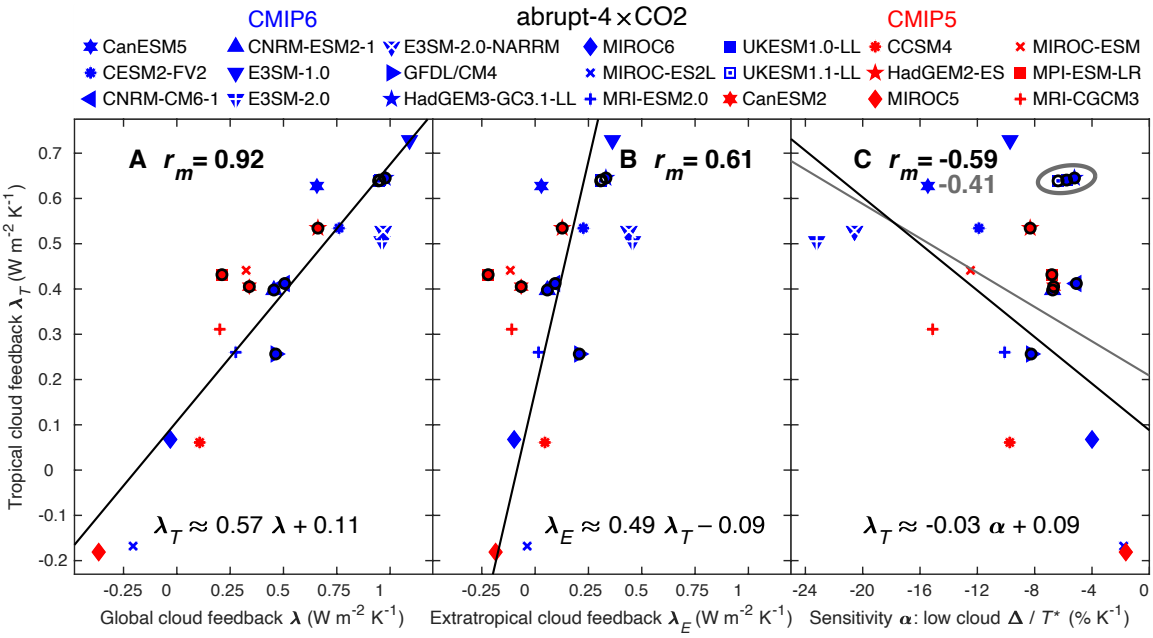

Fig. S8. Same as in Fig. 3 but for the relationships of total cloud radiative feedback (W m^{-2} K^{-1}) in the tropics ($\boldsymbol{\lambda_T}$) with cloud feedbacks over (*A*) the globe ($\boldsymbol{\lambda}$) and (*B*) the extratropics ($\boldsymbol{\lambda_E}$), as well as (*C*) the percentage sensitivity ($\boldsymbol{\alpha}$) of low clouds (% K^{-1}). It should be noted that the intermodel regressions keep *x*-*y* across (*A* and *C*) but are transposed to *y*-*x* in (*B*), and the outliers are marked in (*C*).

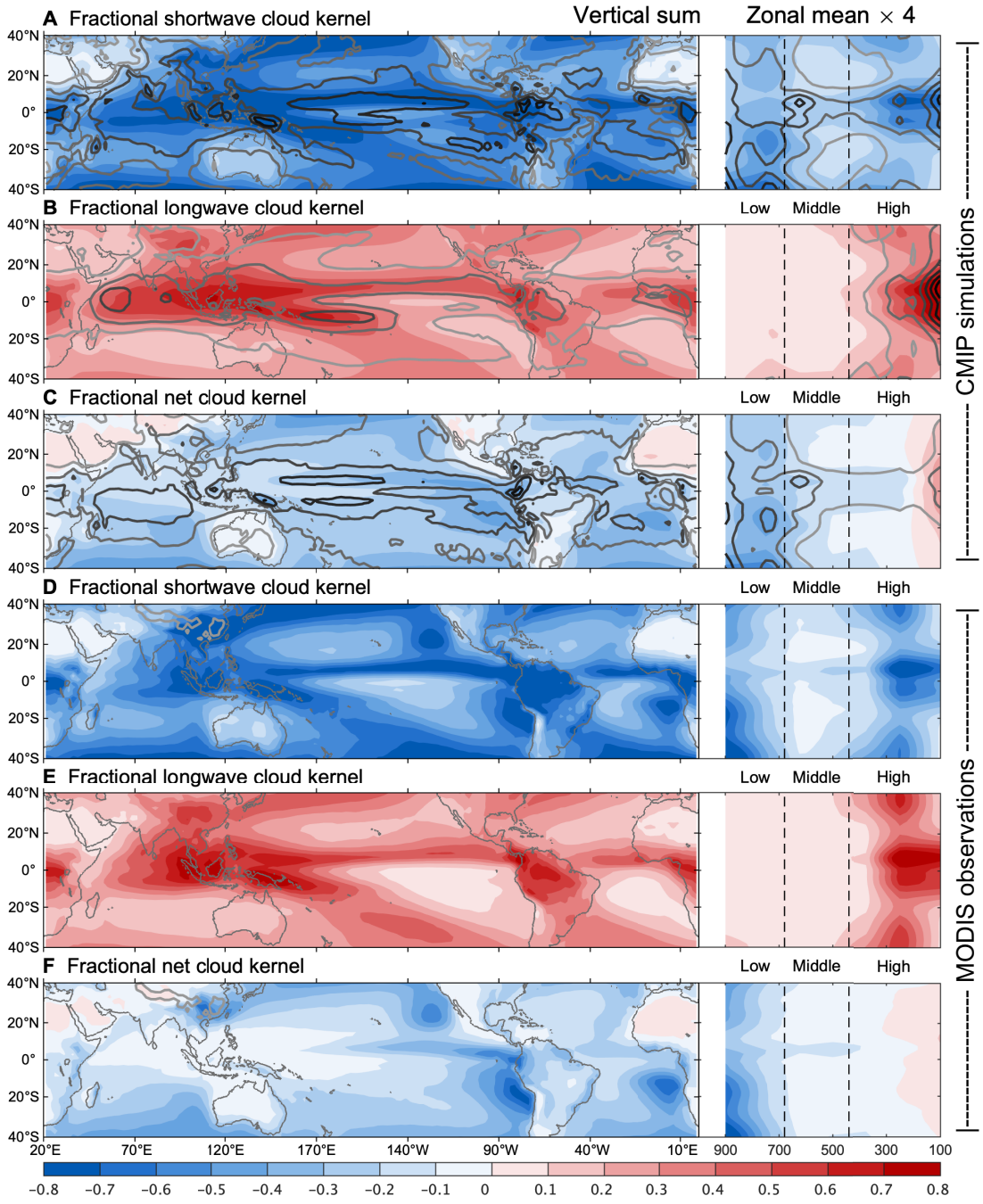

Fig. S9. Horizontal distributions (left) and zonal means (right) of the tropical fractional kernels (W m^{-2} $\%^{-1}$) for the (*A* and *D*) shortwave, (*B* and *E*) longwave, and (*C* and *F*) net radiation, which are calculated using the cloud climatology in (*A* to *C*) the CMIP simulations and (*D* to *F*) the MODIS observations. After summing over all of the optical depths, the vertical sums are calculated for the left panel, and the zonal means for the right panel. The ensemble mean is shown by the shading, and the intermodel spread is by the contours (CI: 0.05 W m^{-2} $\%^{-1}$; darker indicates a greater value). The dashed lines at 440 and 680 hPa divide the cloud types by altitude. Here, the monthly-mean cloud radiative kernels are multiplied by the cloud climatology from the 21 CMIP simulations and the MODIS data during 2003–2022, to compute the unequal spatial weights for the SST pattern effect.

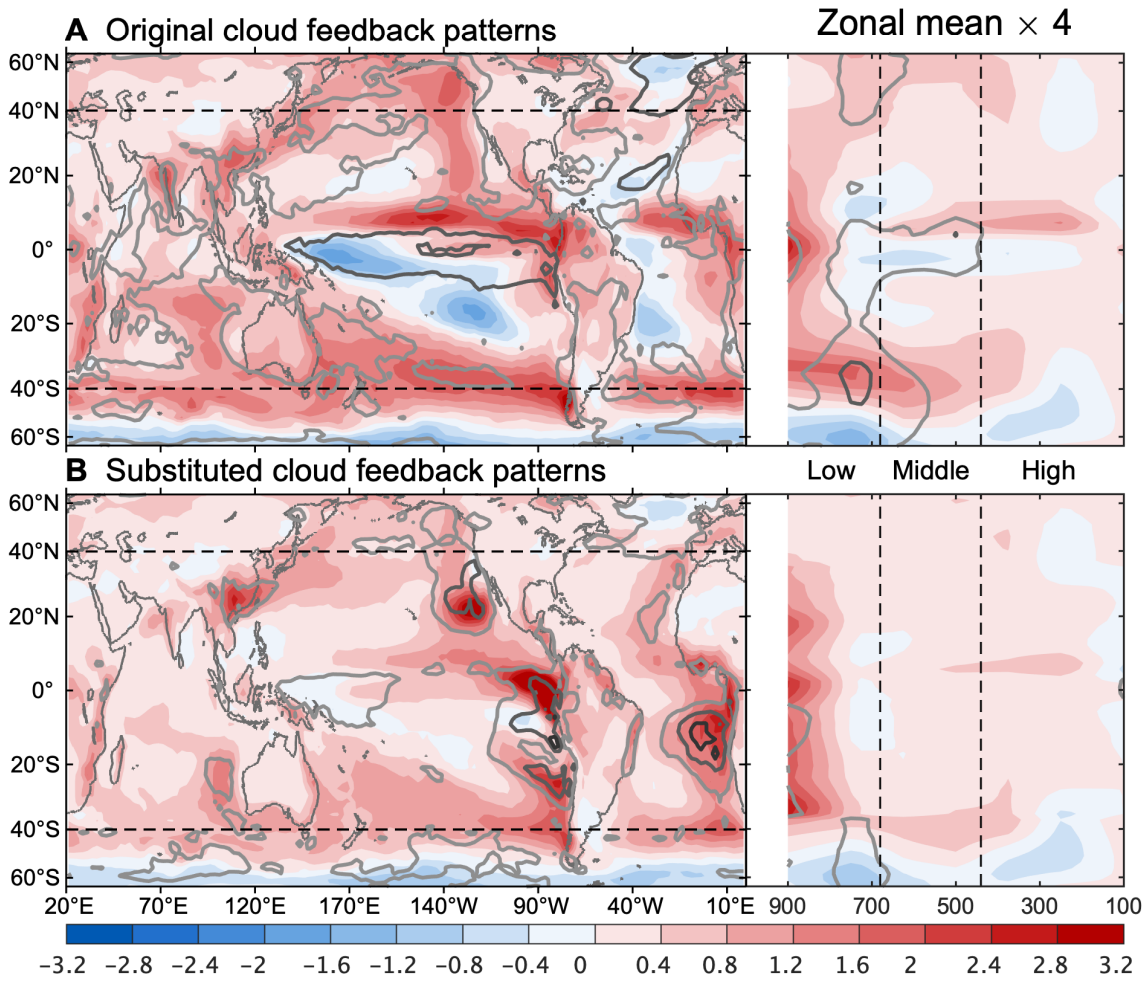

Fig. S10. Comparisons of the horizontal (left) and zonal-mean (right) distributions between the (*A*) original (λ) and (*B*) substituted (λ_s) cloud feedback (W m^{-2} K^{-1}). The ensemble mean (shading) is presented with the intermodel spread (contours, CI: 1 W m^{-2} K^{-1}; darker indicates a greater value). The dashed lines mark the extended tropics for 40°S–40°N and divide the cloud types by altitude at 440 and 680 hPa. Here we use the monthly-mean cloud radiative kernels, SST and cloud observations, and 21 CMIP simulations normalized by the global-mean surface (air) warming.

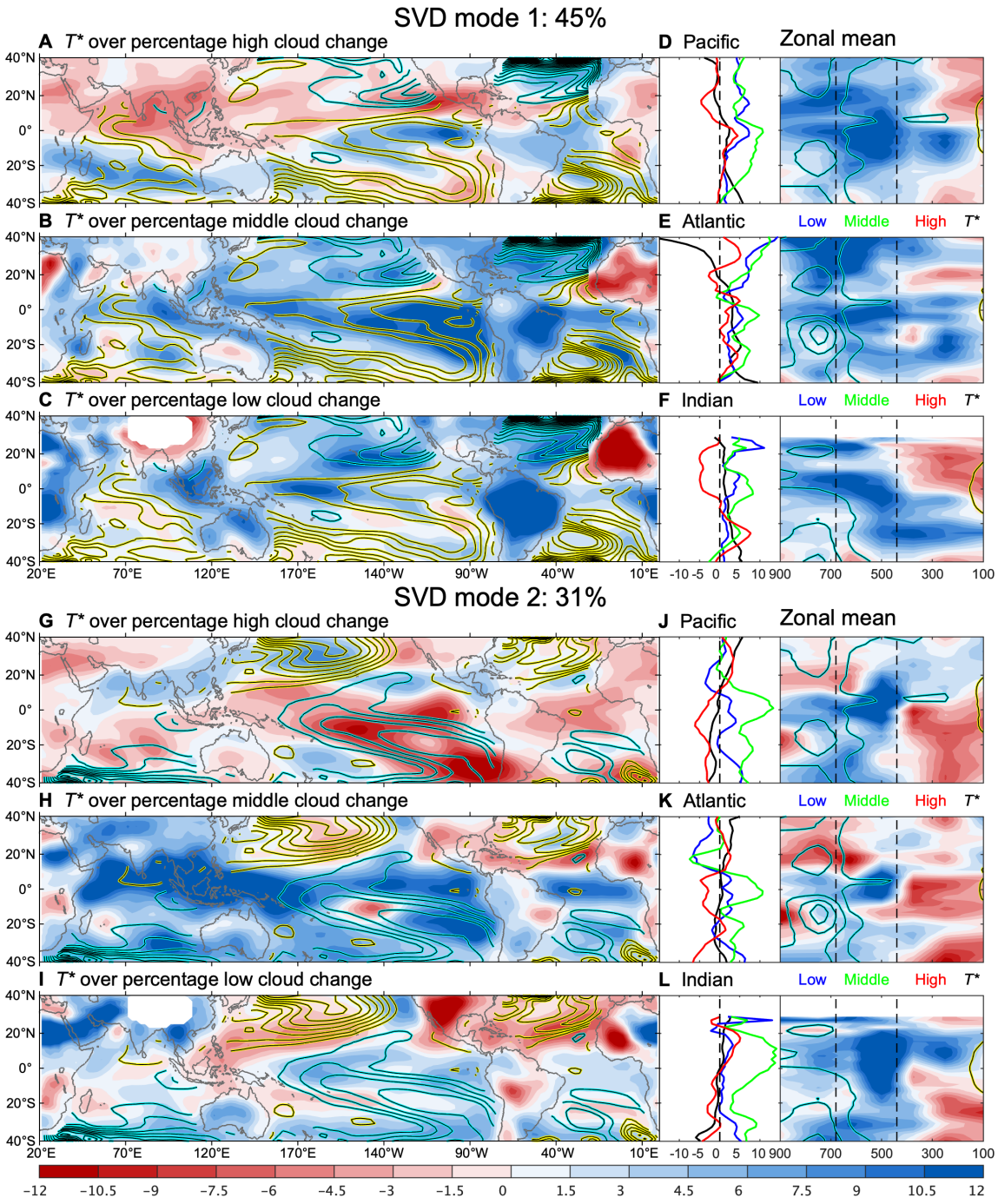

Fig. S11. Unscaled intermodel SVD (*A* to *F*) mode 1 and (*G* to *L*) mode 2 between the *T** anomaly (K) and the anomalous percentage change Δ′ (%) in the tropical (*A* and *G*) high, (*B* and *H*) middle, and (*C* and *I*) low clouds, and the zonal mean modes for the (*D* and *J*) Pacific, (*E* and *K*) Atlantic, and (*F* and *L*) Indian Oceans. Horizontal distributions (*A* to *C* and *G* to *I*) show Δ′ as shading and *T** as contours (CI: 0.1 K; yellow positive, cyan negative; 0 omitted). For zonal means (*D* to *F* and *J* to *L*), the left panel compares cloud-type decompositions with *T**, and the right panel presents clouds (shading) with the simulated fractional net kernel (contours, CI: 0.05 W m^{-2} $\%^{-1}$; yellow positive, cyan negative; 0 omitted). Here we use the 21 CMIP simulations normalized by the global-mean surface (air) warming.

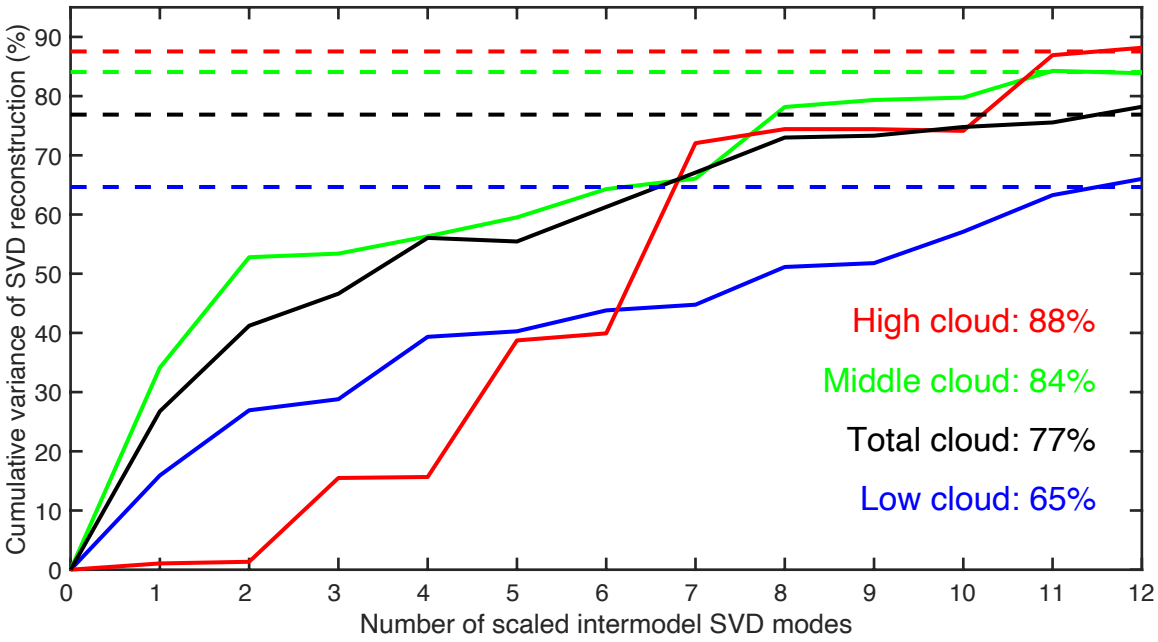

Fig. S12. Cumulative variance (%) of the substituted cloud feedback λ_s explained by the leading SVD modes for only the anomalies associated with the ensemble-mean fractional kernels. The SVD modes are reordered according to the individual variances (direct R^2) by their responsible partial feedbacks, and then linearly combined to compute the cumulative variance as the exclusive R^2 (*Methods*). Here we use the monthly-mean cloud radiative kernels, SST and cloud observations, and 21 CMIP simulations normalized by the global-mean surface (air) warming.

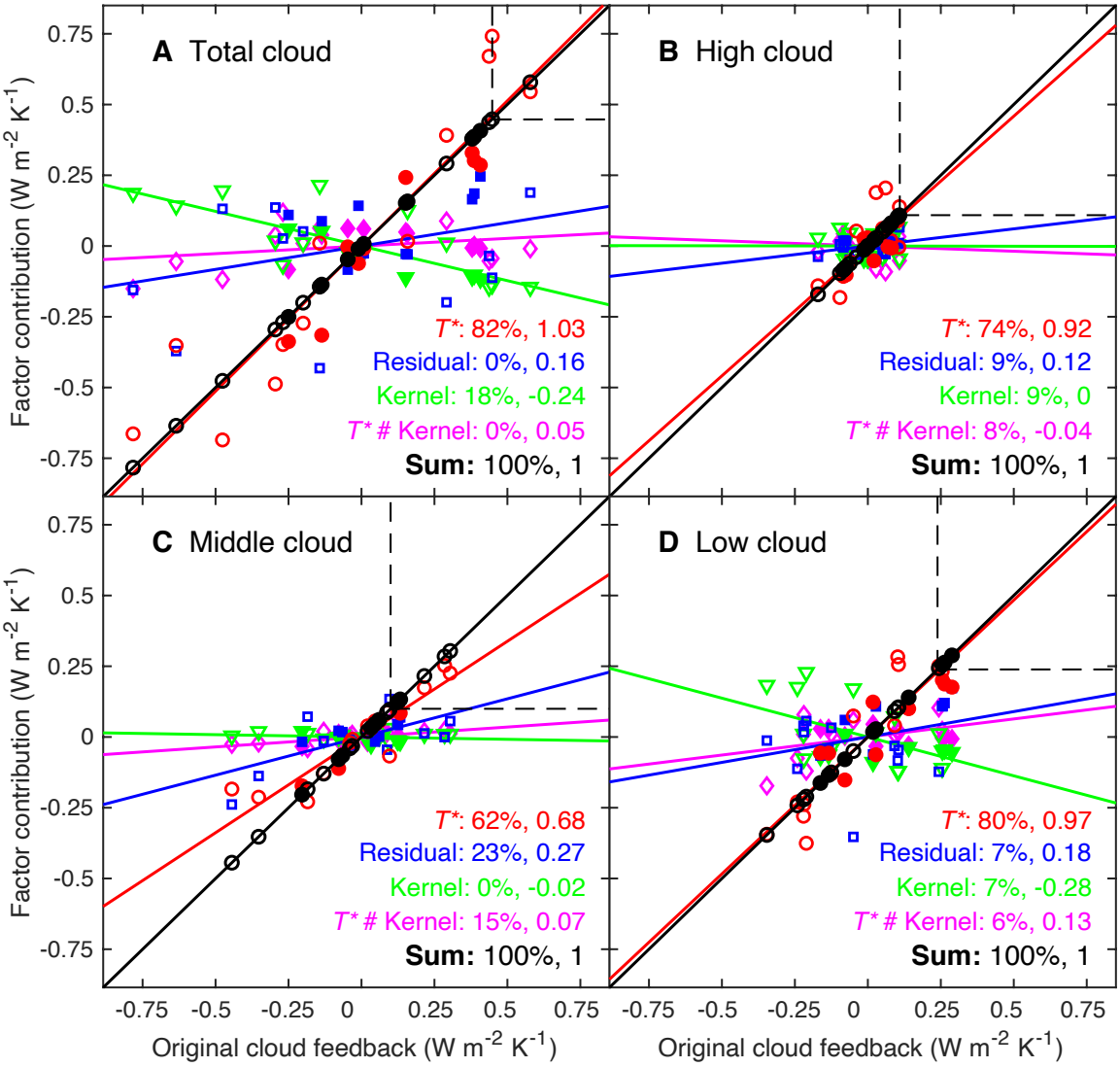

Fig. S13. Same as in Fig. 4 but for the original cloud feedback λ and its factor effects evaluated using the attribution procedure, including the accumulation of the first 12 SVD modes controlled by the T^*, residual factors, fractional kernel biases, and nonlinear T^*-kernel interaction for (*A*) total, (*B*) high, (*C*) middle, and (*D*) low clouds.

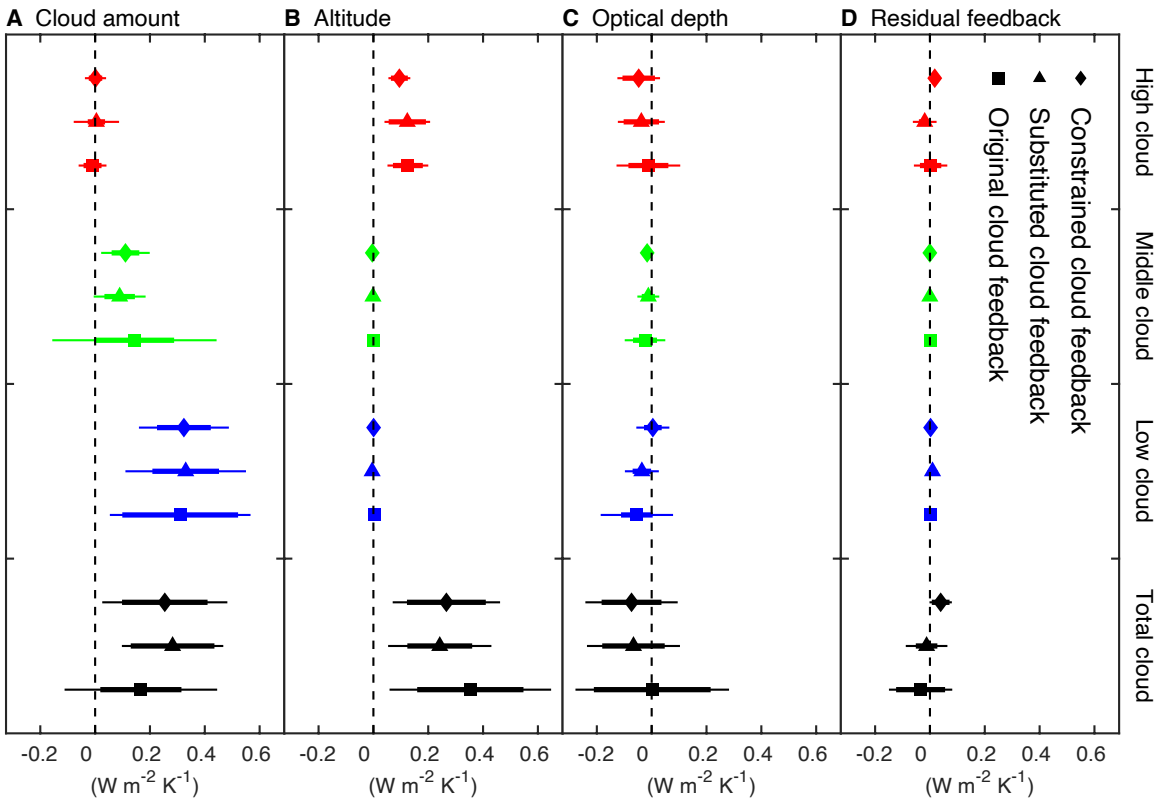

Fig. S14. Decomposed comparisons between the original cloud feedback λ (W m^{-2} K^{-1}) and that constrained in two stages, for (*A*) cloud amount, (*B*) altitude, (*C*) optical depth, and (*D*) residual feedback of all cloud types. For each feedback, the symbol denotes the ensemble mean, with thin and thick error bars spanning the 90% and 66% (~1 standard deviation) confidence intervals, respectively. Here we use the monthly-mean radiative kernels, SST and cloud observations, and 21 CMIP simulations normalized by the global-mean surface (air) warming.

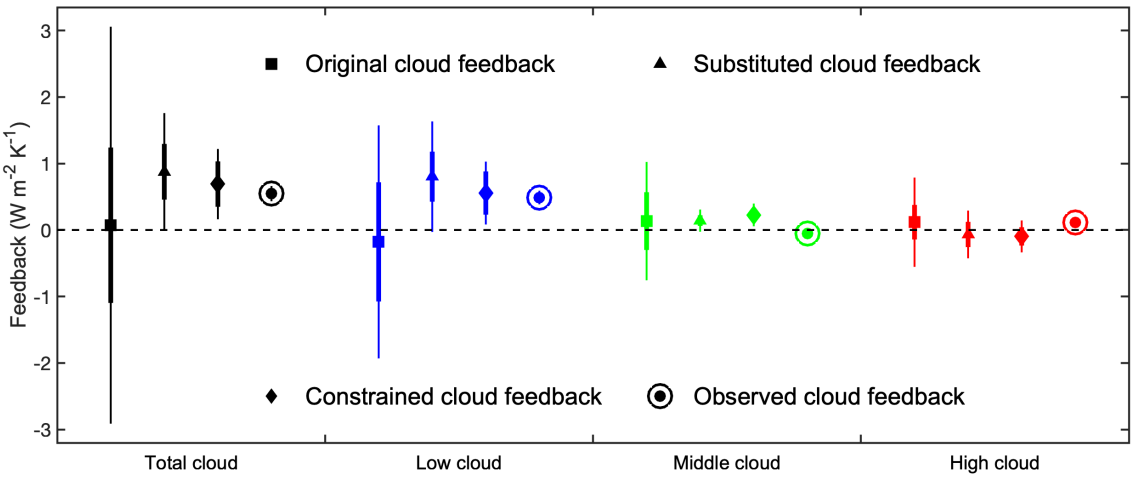

Fig. S15. Same as in Fig. 5*C* but for the tropical cloud feedback computed using the 20 historical simulations during 1986–2005, and its comparison with the observed tropical feedback based on the MODIS clouds and SST suite during 2003–2022.

SM References

1. D. S. Abbot, E. Tziperman, Sea ice, high latitude convection, and equable climates. *Geophys. Res. Lett.* 35, L03702 (2008).
2. S.-P. Xie *et al.*, Global warming pattern formation: Sea surface temperature and rainfall. *J. Clim.* 23, 966–986 (2010).
3. T. Koshiro, H. Kawai, A. T. Noda, Estimated cloud-top entrainment index explains positive low-cloud-cover feedback. *Proc. Nat. Acad. Sci.* 119, e2200635119 (2022).
4. I. N. Williams, R. T. Pierrehumbert, Observational evidence against strongly stabilizing tropical cloud feedbacks. *Geophys. Res. Lett.* 44, 1503–1510 (2017).
5. S. Bony *et al.*, Thermodynamic control of anvil cloud amount. *Proc. Natl. Acad. Sci. USA* 113, 8927–8932 (2016).
6. P. Ceppi, F. Brient, M. D. Zelinka, D. L. Hartmann, Cloud feedback mechanisms and their representation in global climate models. *WIREs Clim. Change* 8, e465 (2017).
7. M. Saint-Lu, S. Bony, J.-L. Dufresne, Observational evidence for a stability Iris effect in the tropics. *Geophys. Res. Lett.* 47, e2020GL089059 (2020).
8. C. Zhou, M. D. Zelinka, S. A. Klein, Analyzing the dependence of global cloud feedback on the spatial pattern of sea surface temperature change with a Green's function approach. *J. Adv. Model. Earth Syst.* 9, 2174–2189 (2017).
9. P. Ceppi, P. Nowack, Observational evidence that cloud feedback amplifies global warming. *Proc. Natl. Acad. Sci. USA* 118, e2026290118 (2021).
10. H. Zhang *et al.*, Low-cloud feedback in CAM5-CLUBB: Physical mechanisms and parameter sensitivity analysis. *J. Adv. Model. Earth Syst.* 10, 2844–2864 (2018).
11. S. A. Klein, A. Hall, J. R. Norris, R. Pincus, Low-cloud feedbacks from cloud-controlling factors: A review. *Surv. Geophys.* 38, 1307–1329 (2017).
12. T. A. Myers *et al.*, Observational constraints on low cloud feedback reduce uncertainty of climate sensitivity. *Nat. Clim. Change* 11, 501–507 (2021).
13. R. Scott *et al.*, Observed sensitivity of low-cloud radiative effects to meteorological perturbations over the global oceans. *J. Clim.* 33, 7717–7734 (2020).
14. S. Wilson Kemsley *et al.*, A systematic evaluation of high-cloud controlling factors. *Atmos. Chem. Phys.* 24, 8295–8316 (2024).
15. M. D. Zelinka, S. A. Klein, D. L. Hartmann, Computing and partitioning cloud feedbacks using cloud property histograms. Part I: Cloud radiative kernels. *J. Clim.* 25, 3715–3735 (2012).

16. S. C. Sherwood, S. Bony, J.-L. Dufresne, Spread in model climate sensitivity traced to atmospheric convective mixing. *Nature* 505, 37–42 (2014).
17. C. Zhou, M. D. Zelinka, S. A. Klein, Impact of decadal cloud variations on the Earth's energy budget. *Nat. Geosci.* 9, 871–874 (2016).
18. R. Pincus, S. Platnick, S. A. Ackerman, R. S. Hemler, R. J. P. Hofmann, Reconciling simulated and observed views of clouds: MODIS, ISCCP, and the limits of instrument simulators. *J. Clim.* 25, 4699–4720 (2012).
19. M. D. Zelinka *et al.*, Causes of higher climate sensitivity in CMIP6 models. *Geophys. Res. Lett.* 47, e2019GL085782 (2020).
20. J. Feng, J. Ma, Improved decomposition of cloud feedback and corresponding pattern change under uniform surface ocean warming: I. Anomalous mean method. *Geosci. Lett.* 12, 35, doi:10.1186/s40562-025-00407-4 (2025).
21. Q. Hu, On the uniqueness of the singular value decomposition in meteorological applications. *J. Clim.* 10, 1762–1766 (1997).
22. H. Murakami *et al.*, Detected climatic change in global distribution of tropical cyclones. *Proc. Natl. Acad. Sci. USA* 117, 10706–10714 (2020).
23. J. Ma, S.-P. Xie, Regional patterns of sea surface temperature change: A source of uncertainty in future projections of precipitation and atmospheric circulation. *J. Clim.* 26, 2482–2501 (2013).
24. J. Ma, S.-P. Xie, Y. Kosaka, Mechanisms for tropical tropospheric circulation change in response to global warming. *J. Clim.* 25, 2979–2994 (2012).
25. J. Zhang, J. Ma, J. Che, Z.-Q. Zhou, G. Gao, Surface warming patterns dominate the uncertainty in global water vapor plus lapse rate feedback. *Acta Oceanol. Sin.* 39, 1–9 (2020).